

Instability of Nano- and Microscale Liquid Metal Filaments: Transition from Single Droplet Collapse to Multidroplet Breakup

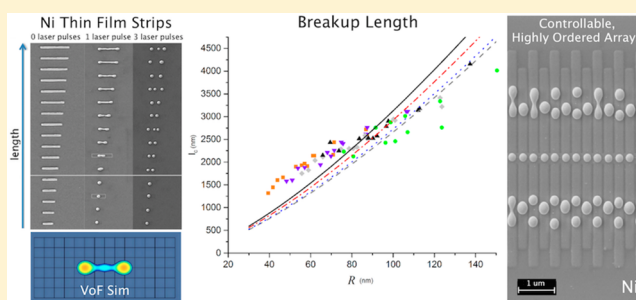
C. A. Hartnett,[†] K. Mahady,[§] J. D. Fowlkes,^{‡,||} S. Afkhami,[§] L. Kondic,[§] and P. D. Rack^{*,‡,||}

[†]Department of Physics & Astronomy and [‡]Department of Materials Science & Engineering, University of Tennessee, Knoxville, Tennessee 37996, United States

[§]Department of Mathematical Sciences, New Jersey Institute of Technology, Newark, New Jersey 07102, United States

^{||}Center for Nanophase Materials Sciences, Nanofabrication Research Laboratory, Oak Ridge National Laboratory, Oak Ridge, Tennessee 37831, United States

ABSTRACT: We carry out experimental and numerical studies to investigate the collapse and breakup of finite size, nano- and microscale, liquid metal filaments supported on a substrate. We find the critical dimensions below which filaments do not break up but rather collapse to a single droplet. The transition from collapse to breakup can be described as a competition between two fluid dynamic phenomena: the capillary driven end retraction and the Rayleigh–Plateau type instability mechanism that drives the breakup. We focus on the unique spatial and temporal transition region between these two phenomena using patterned metallic thin film strips and pulsed-laser-induced dewetting. The experimental results are compared to an analytical model proposed by Driessen et al. and modified to include substrate interactions. In addition, we report the results of numerical simulations based on a volume-of-fluid method to provide additional insight and highlight the importance of liquid metal resolidification, which reduces inertial effects.



1. INTRODUCTION

For many applications, controlling the placement and composition of metallic nanostructures is crucial. For instance, the incorporation of plasmonic nanoparticles into photovoltaic devices has led to increased efficiency,^{1,2} and importantly the surface plasmon resonance between metallic nanostructures depends on coordination, size, and spacing.^{3,4} Other applications include bionanotechnology and sensing, where functionalized Au nanoparticles bind to specific DNA markers, permitting binding detection.⁵ The potential applications for organized metallic nanostructures are wide-ranging and include Raman spectroscopy,^{6,7} catalysis,⁸ photonics,⁹ and spintronics.¹⁰ One strategy to create and organize structures at the nanoscale is harnessing a material's inherent self-assembly mechanisms. The physical properties of liquid metals, such as low viscosity and high surface energy, and the ability to lithographically pattern nanoscale features, create an intriguing platform to study the governing liquid-state dewetting dynamics,¹¹ such as liquid instabilities,¹² with the goal of directing the assembly of precise, coordinated nanostructures in one¹³ and two¹⁴ dimensions.

In this work we observe that liquid metal filaments below a critical length, l_c , collapse to a single droplet; however, as a filament length increases, a threshold is crossed where multidroplet breakup results. As the breakup is a Rayleigh–Plateau-like instability, this threshold is a function of the filament radius of curvature, R . Herein we focus on the unique

spatial and temporal transition region between the two regimes. We show the transition can be described as a competition between two fluid dynamic phenomena: (1) capillary-induced retraction of the filament axial ends promoting the collapse to a single droplet and (2) filament breakup into multiple droplets due to the growth of varicose surface instabilities similar to the Rayleigh–Plateau (R – P) mechanism.

To investigate this competition, we utilize established nanofabrication techniques and pulsed laser-induced dewetting (PliD).¹⁴ With these methods it is experimentally possible to precisely control the initial far-from-equilibrium geometry and the liquid lifetime via nanosecond laser melting. The finite extent of a filament geometry and, as we will demonstrate, the temperature and liquid lifetime have profound effects on the dewetting dynamics. We first give an overview of the experimental results and then compare them with relevant hydrodynamic models. Finally, we compare the experimental results with direct numerical computations of the full Navier–Stokes equations based on the volume-of-fluid (VoF) interface tracking method.¹⁵

Received: September 26, 2015

Revised: November 17, 2015

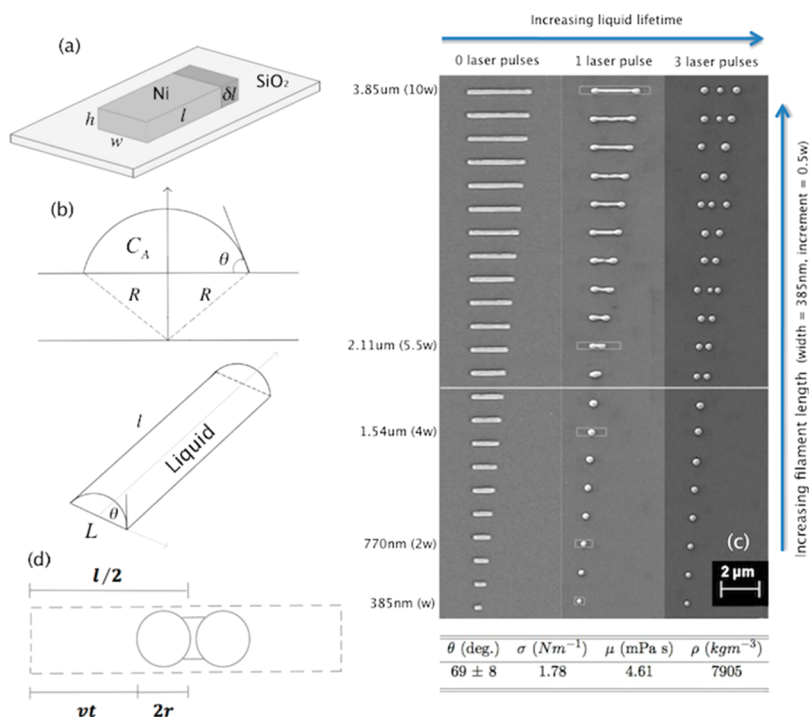


Figure 1. (a) Illustration of the patterned Ni TFS on SiO_2 , having thickness, h , width, w , and length, l , and increment length, $\delta l = (w/2)$. Thickness ranges from 10 ± 1 to 30 ± 1 nm in 5 nm increments. (b) Geometry of the substrate-supported liquid metal filament with equilibrium contact angle, θ , cross-sectional area, C_A , and radius of curvature, R . (c) Scanning electron microscope (SEM) images of the Ni TFS increasing in length from bottom to top, initially square with sides, l_0 , equal to the width. Liquid lifetime increases from left to right as a function of the number of laser pulses. At a critical length, l_c (horizontal line), the filament breaks up into multiple droplets rather than collapsing into a single droplet. For this particular example $h = 20 \pm 1$ nm, $w = 437 \pm 12$ nm, $C_A = 8740 \pm 498$ nm², and l_c is ~ 2.1 μ m. Included are relevant material properties of Ni at the melting temperature, $T_m = 1728$ K, the equilibrium contact angle, θ ,¹³ the surface tension, σ ,¹⁸ the viscosity, μ ,¹⁹ and the density, ρ .²⁰ (d) Top-down view of a retracting filament the instant before the accumulating edge droplets, of radius r and traveling at velocity v , merge to form a single droplet. The filament length where the end droplets do not have sufficient time to retract half the length and merge when breakup occurs is the critical length (breakup time equals collapse time); this time condition is expressed as eq 1.

2. EXPERIMENTAL SECTION

Electron beam lithography (EBL) was used to pattern a mask of rectangular strips of increasing width ($w = 136$ – 668 nm) and length ($l = 0.135$ – 12.3 μ m) using a positive tone resist, poly(methyl methacrylate) (PMMA), on a 100 nm SiO_2 surface that was thermally grown on a prime (100) Si wafer. Nickel (Ni) was subsequently deposited using dc magnetron sputtering with a thickness, h , and ranged from 10 ± 1 to 30 ± 1 nm in 5 nm increments. Figure 1a illustrates the resultant Ni thin film strip (TFS) geometry on oxide, characterized by the cross-sectional area, hw .

A krypton fluoride (KrF) excimer laser, wavelength 248 nm, energy range 220 – 300 ± 10 mJ cm^{-2} , and pulse width of 18 ± 2 ns fwhm, was used to melt the Ni TFS. Figure 1b demonstrates the substrate-supported, liquid metal filament geometry that results from the laser melting. The amount of time a Ni TFS is in the liquid state, its liquid lifetime, is dependent on the energy fluence delivered by a laser shot and the thermal and optical properties of the Ni, the supporting SiO_2 layer, and the underlying Si substrate. The area of the laser spot is ~ 1 cm^2 , which is much larger than the ~ 1 mm^2 area containing the sample, thus ensuring a homogeneous fluence. Figure 2 is a collection of numerical simulations modeling the surface temperature of the Ni thin film supported on 100 nm SiO_2 on Si, exposed to one 250 mJ cm^{-2} laser shot.¹⁶ Because of the finite liquid lifetime per laser pulse and rapid cooling, a series of individual laser pulses can be used to control the dewetting evolution and interrogate morphological changes of the liquid filament.¹⁷

3. MODEL AND SIMULATION METHODS

3.1. Model. Here we estimate several quantities to identify the relevant fluid dynamic regime for our experiments. As

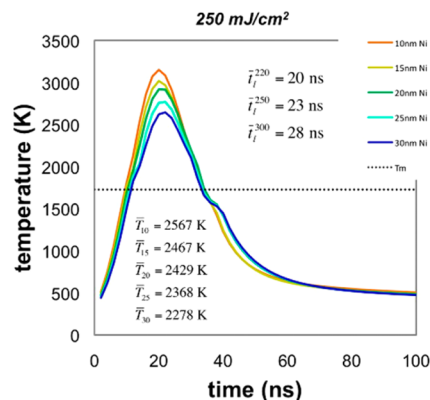


Figure 2. Simulated surface temperatures of a Ni thin film on 100 nm SiO_2 on Si during and after the absorption of a single KrF laser pulse with a fluence of 250 mJ cm^{-2} . The liquid lifetime, t_l , is the amount of time spent at or above the Ni melting temperature, 1728 K (dotted line). Insets are the average liquid lifetimes at three laser fluences, 220, 250, and 300 mJ cm^{-2} , and the average temperatures during the liquid lifetime after a single laser pulse with a fluence of 250 mJ cm^{-2} .

described, the experimental length scales that are operative are thicknesses at the tens of nanometer range, widths at the hundreds of nanometer range, and lengths ranging from hundreds of nanometers to tens of micrometers, well below the capillary length, $\lambda_c = (\sigma/\rho g)^{1/2}$, of ~ 1 mm for liquid Ni. Therefore, gravitational effects are not important. The

Ohnesorge number, $Oh = \mu(\rho\sigma R)^{-1/2}$, the ratio of viscous to inertial and surface tension forces, is on the order ~ 0.1 . The R–P instability is expected to be an influential mechanism within the range of $0.05 < Oh < 2$ for viscous filaments.²¹ Driessen et al.²¹ demonstrated that filaments dominated by inertia/surface tension ($Oh < 0.05$) break up by end pinch-off, and if viscosity dominates ($Oh > 2$), the filaments are stable with respect to the R–P instability and collapse to a single droplet independent of length. On the basis of our working Oh regime (~ 0.1) (see Table 1 and Figure 4b), we expect the R–P

Table 1. Variation of the Ohnesorge Number in the Experiment Due to the Temperature-Dependent Material Properties of Viscosity, Surface Tension, and Density at the Filament Radii Minimum and Maximum [44 nm, 150 nm]

	1728 K	2500 K
Oh	[0.185, 0.100]	[0.103, 0.056]

mechanism to be operative and thus the transition from collapse to breakup to be sensitive to the aspect ratio ($\Gamma = l/2R$) of the substrate supported filament.

When a patterned Ni TFS melts, the initially rectangular cross-sectional area, hw , forms a truncated cylinder of equal cross-sectional area, $C_A = R^2A(\theta)$, where the radius of curvature, R , depends on the equilibrium contact angle between the liquid metal and the SiO_2 substrate and $A(\theta) = \theta - \sin\theta \cos\theta$ (see Figure 1b).¹¹ The amount of time it takes for an Ni TFS to transition to a truncated cylinder during laser melting is ~ 1 – 2 ns.¹²

At filament lengths below where breakup occurs, retracting axial ends travel half the filament length to merge/collapse to form single droplets. For a filament to collapse to a single droplet the amount of time the filament axial ends have to travel and successfully merge must be less than the time necessary for the development of varicose instabilities that lead to R–P breakup. The time condition between collapse and breakup can be expressed as a critical, axial end retraction time

$$t_c = \left(\frac{l_c}{2} - 2r \right) v^{-1} \quad (1)$$

where $l_c/2$ is half the filament length at the critical length where transition occurs, r is the radius of the accumulating droplet at the retracting axial end, and v is the retracting end velocity (see Figure 1d).

The capillary velocity, $v_{\text{cap}} = (\sigma/\rho R)^{1/2}$, ranges from 38 to 71 ms^{-1} at the melting temperature for the filament radii maximum and minimum (150 and 44 nm), respectively. The axial end retraction velocity was experimentally estimated by measuring the retraction distance of the TFS after exposure to a single laser pulse and normalized to the average simulated liquid lifetime (24 ns). The range of experimentally determined velocities, spanning the range of filament radii (150 to 44 nm), is 36–19 ms^{-1} , respectively, with an average of 29 ms^{-1} . Counter to the prediction of the capillary velocities, the experimental retraction velocities are smaller and the dependence on filament radius is reversed at small radii. These experimental findings are attributed to energy losses due to viscous dissipation at the filament–substrate interface, the temperature-dependent material properties, and solidification effects that will be discussed later. Furthermore, we are neglecting the effect that material accumulation at the filaments ends may have during retraction. The velocity was also

simulated via the VoF approach, described later in this section, at 1728 and 2500 K and radii range of 25–87 nm. The simulations resulted in average velocities of 34 and 41 ms^{-1} at 1728 and 2500 K, respectively. Figure 3 compares the capillary,

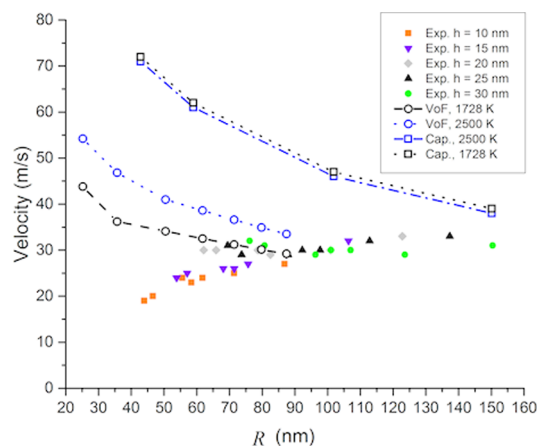


Figure 3. Experimental retraction velocities measured after one liquid lifetime, grouped by initial TFS thickness, and compared to the theoretical capillary velocity and VoF simulation estimates at two temperatures, 1728 and 2500 K. The average experimental retraction velocity is 29 ms^{-1} . For the analytical model, eq 6, a value of 30 ms^{-1} was chosen to approximate the experimental results. The experimental velocities are noticeably lower at smaller filament radii, which is in contrast to the VoF and capillary velocity behavior. Future work should explore the reasons for this difference; we anticipate that temperature-dependent material properties may play an important role in eventual explanation.

experimental, and VoF velocity data. The capillary, experimental, and VoF velocities are of similar order, which is reassuring. For simplicity we use a constant, average velocity of 30 ms^{-1} in our analytical model below.

The accumulating droplet at the retracting axial end creates a rim, the extent of which can be estimated by the Stokes length, $L_s = \mu^2/(\rho\sigma)$, and can have a stabilizing effect on the filament if it approaches half the filament length. That is, if the two rims that form at the filament ends overlap, they can induce collapse of the filament homogeneously to a single droplet. The Stokes length for the considered experiment is on the order of a few nanometers, so the retracting axial droplets are immune to rim interactions.

Driessen et al. outlined a similar argument for single droplet collapse for (nonmetallic) free viscous jets (filaments) (not supported on a substrate). To do so, Driessen et al. utilized a convenient framework to describe the system, which we will modify to include the effects of the supporting substrate. The filament is described in terms of its aspect ratio, $\Gamma = l/2R$. At the critical length the retracting axial ends each accumulate half the volume of the filament, forming an end droplet with radius

$$r = \left(\frac{3}{4} \Gamma_c \right)^{1/3} R \quad (2)$$

The critical axial end retraction time, given by eq 1, can be rewritten as a function of the aspect ratio and radius of curvature, R , by combining it with eq 2:

$$t_c = R(\Gamma_c - (6\Gamma_c)^{1/3})v^{-1} \quad (3)$$

For a free filament in air, of radius R_0 , the varicose surface perturbation of maximum growth rate causes breakup. The wavelength of this most unstable perturbation is predicted by linear stability analysis (LSA) of the R–P instability to be²²

$$\Lambda_m = 2\pi\sqrt{2R_0} \quad (4)$$

As the free filament is destabilized by the growth of the surface perturbation, the resultant distribution of droplets should be spaced approximately equal to the wavelength Λ_m ; that is, the final droplet distribution should scale with R_0 . Assuming that the LSA of R–P instability can be extended to the nonlinear regime, the time needed for a R–P type surface perturbation to grow to an amplitude^{11,21} comparable to that of the filament radius is

$$t_b = \frac{1}{\omega} \ln\left(\frac{R}{\delta}\right) \quad (5)$$

Here the initial amplitude of the surface perturbation is represented by δ , and ω is the growth rate of the fastest growing perturbation.

For the nanoscale liquid metals considered here, the initial perturbation amplitude is assumed to be the van der Waals radius of a Ni atom ($\delta = 0.2$ nm).²³ This is in contrast to Driessen et al., who chose their perturbation to be a function of radius, $\delta = \varepsilon R$, with $\varepsilon = 0.01$; this value was chosen as a fit parameter to their experimental data. Alternatively, Diez et al.¹¹ used an ε value of 0.001 as their initial, infinitesimal perturbation value in a fully nonlinear time-dependent simulation of finite length filaments and finding the breakup to be dominated by the pinching off of droplets at the axial ends. Our constant δ value of the van der Waal radius, and filament radii range, yields effective ε values ranging from 0.0013 to 0.0045 and commensurate to both approaches.

The transition from single droplets to multiple droplets can therefore be described as a competition between two fluid dynamic time scales, that of collapse due to axial end retraction and the R–P instability time for breakup. An expression for the critical aspect ratio can then be found by equating eqs 3 and 5:

$$R(\Gamma_c - (6\Gamma_c)^{1/3})v^{-1} - \frac{1}{\omega_s} \ln\left(\frac{R}{\delta}\right) = 0 \quad (6)$$

However, the Driessen et al. description is that of a free filament. We extend their description to that of a filament supported on and partially wetting a solid surface. Therefore, ω is replaced with ω_s , the growth rate of the fastest growing perturbation for liquid filaments supported on a solid substrate.

Brochard-Wyart and Redon²⁴ estimated the relaxation times of the varicose modes of a liquid filament with circular cross section on a flat solid surface and found that modes below a wave vector, q , are unstable. They predicted the relaxation times of the instabilities in two regimes: a viscous regime, where viscous dissipation is the dominant hydrodynamic quantity, and the viscoinertial regime, appropriate for low viscosity and large contact angle fluids. For the viscous regime they determined the relaxation times for all q as

$$\omega^{\text{vis}} = \frac{\sigma}{3\mu c} \theta^3 \frac{q}{1 + 4/q^2 L^2} \left(-\frac{2}{Lq} + \tanh\frac{Lq}{2} \right) \quad (7)$$

where the filament substrate-supported width is $L = 2R \sin \theta$ (see Figure 1b) and c is a logarithmic factor reflecting the singularity near the contact line, on the order 10, and can be

treated as a constant.²⁵ The fastest growing mode occurs for $qL \approx 1.421$,¹¹ therefore

$$\omega_s^{\text{vis}} = 0.379 \frac{\sigma}{30\mu} \frac{\theta^3}{2R \sin \theta} \quad (8)$$

For the viscoinertial regime, Brochard-Wyart and Redon determined the relaxation times for all q as

$$\omega^{\text{viscoin}} = \left(\frac{\theta}{L}\right)^{4/3} \left(\frac{\sigma}{\mu\rho}\right)^{1/3} \times \frac{(-1 + (qL/2) \tanh(qL/2))^{1/3} (1 + qL/2)^{2/3}}{(1 + 4/q^2 L^2)^{2/3}} \quad (9)$$

Once again the fastest growing mode has a value of $qL \approx 1.421$, therefore

$$\omega_s^{\text{viscoin}} = 0.317 \left(\frac{\theta}{2R \sin \theta}\right)^{4/3} \left(\frac{\sigma^2}{\mu\rho}\right)^{1/3} \quad (10)$$

3.2. Simulation Methods. In the final section we compare the experimental results with the ones obtained by fully nonlinear simulations based on a VoF method. By solving the three-dimensional Navier–Stokes (N–S) equations, these simulations provide additional insight regarding the competing instability mechanisms. It is assumed that the fluid flow can be modeled as an isothermal Newtonian fluid obeying the N–S equations.

$$\rho \frac{D\mathbf{u}}{Dt} = -\nabla p + \nabla \cdot (\mu(\nabla\mathbf{u} + \nabla\mathbf{u}^T)) + \sigma\kappa\delta_s \mathbf{n} \quad (11)$$

$$\nabla \cdot \mathbf{u} = 0 \quad (12)$$

where $\mathbf{u} = (u, v, w)$ is the velocity field, p is the pressure, κ is the curvature of the fluid–vapor interface, and $\delta_s \mathbf{n}$ denotes the normal vector of the liquid interface. A contact angle of 90° is imposed during the simulations. Experimental results could not be reproduced without taking contact line slip and laser melting/solidification effects into account. The contact line slip is represented by a slip condition,

$$(u, w)|_{y=0} = \lambda \partial_y (u, w)|_{y=0} \quad (13)$$

where λ denotes the slip length, and (u, w) are the in-plane components of velocity. To represent liquid solidification, we implement a simple model, such that the fluid motion completely stops after a liquid lifetime, t_l . Therefore, we put

$$\mathbf{u}(\mathbf{x}, nt_l) = 0, \quad \forall \mathbf{x} \text{ and } n \in \mathbb{Z} \quad (14)$$

After the “freeze”, the liquid is allowed to again evolve according to eq 11, mimicking melting and solidification as a result of multiple laser pulses.

The open-source computational fluid dynamics software package Gerris was used for the simulations.²⁶ Spatial discretization is accomplished using an adaptive octree. The adaptive mesh resolves the fluid–vapor interface with a resolution of ~ 1 nm, and regions of high curvature are resolved to ~ 0.5 nm. The VoF approach tracks the fluid phase of each point in space by introducing a volume fraction function, which states the fraction of each computational cell occupied by the liquid phase. Viscosity and density depend on the volume fraction function by assignment of the appropriate

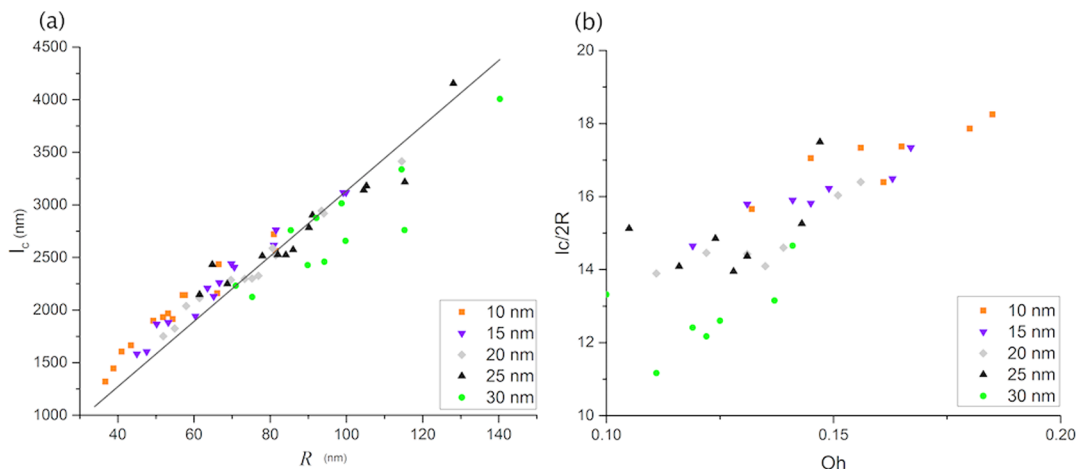


Figure 4. (a) Average experimental l_c colored by initial film thickness. Samples were irradiated with 5 laser pulses using a KrF laser (wavelength 248 nm) at a fluence of 250 mJ cm^{-2} to ensure final droplet morphology (sufficient cumulative liquid lifetime). The linear best-fit parameter is $\alpha' = 31.27$, with 95% confidence bounds [30.52, 32.02]. (b) Critical aspect ratio ($\Gamma_c = l_c/2R$) versus the Ohnesorge number (Oh).

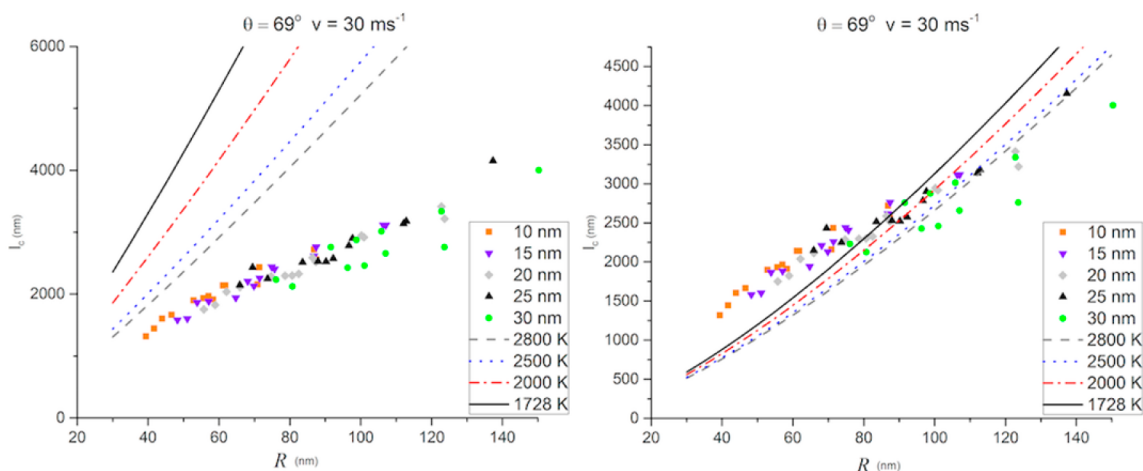


Figure 5. Experimentally measured critical lengths, grouped by initial TFS thickness, compared to the solutions of eq 6 using the viscous and viscoinertial growth rates and at several temperatures. (a) Viscous regime, eq 8. (b) Viscoinertial regime, eq 10. In both cases, (a) and (b), the viscosity and surface tension vary with temperature, the contact angle, 69° , and velocity, 30 ms^{-1} , remain constant.

liquid and vapor values. In order to diminish the effect of the surrounding vapor, we set $\mu_v = \mu/100$ and $\rho_v = \rho/20$.

4. RESULTS AND DISCUSSION

4.1. Experiment and Model. Figure 4a is a plot of average l_c vs R for different thickness and width combinations explored in the experiment. For the 65 data points that were explored (five thicknesses ranging from 10 to 30 nm thick and for each thickness 13 widths ranging from 135 to 665 nm), each data point represents an average of six measurements. We observe that the critical breakup length, to some extent, follows the phenomenological scaling law $l_c = \alpha R = [\alpha(A(\theta)^{-1}C_A)]^{1/2} = \alpha'(C_A)^{1/2}$. This type of scaling law is consistent with that expected for a R–P instability. As is evident in Figure 4a, the linear best-fit line (forced through the origin) appears to underestimate the measured l_c at small cross-sectional area and slightly overestimates it at higher cross-sectional area. We will discuss the origins of these trends at the end of this section. Also shown in Figure 4 is a plot of aspect ratio of the filament at the critical length versus the Ohnesorge number, calculated at the melting temperature.

In Figure 5a, we plot the solutions to eq 6 using the viscous regime fastest growth rate, eq 8, and compare them to the experimental data. In Figure 5b we plot the solutions to eq 6 using the viscoinertial regime fastest growth rate, eq 10, and compare them to the experimental data. We use an axial end retraction velocity of 30 ms^{-1} and a contact angle of 69° , consistent with the experimental value for velocity and the measured equilibrium contact angle for liquid Ni on SiO_2 . As described earlier, the initial varicose perturbation amplitude is chosen to be $\delta = 0.2 \text{ nm}$.

To demonstrate how temperature changes the solutions to eq 6, three additional temperatures are plotted in Figure 5 (2000, 2500, and 2800 K) where the temperature-dependent viscosity and surface energy are used. Noticeably, the agreement improves at higher average liquid temperatures (l_c and slope decreases). The range of Ohnesorge numbers for our experiments and the functionality of Γ_c on Oh are suggestive of the viscoinertial regime; thus while the trends are similar, it is not surprising that the viscous model does not fit the experiments well.

Overall, the experimental data fit well with the viscoinertial solutions. Such a finding is reasonable, based on the Ohnesorge

number, and generally validates that the breakup of these nano- and microscale liquid filaments can be described as a competition between a R–P type instability and the axial collapse of a filament. Notably at larger filament radii the model overestimates the critical length relative to the experimental data, which could be due to a decrease in velocity because of larger filament radius and therefore lower capillary velocity. Additionally, our thermal model neglects geometric effects on the cooling rates; thus we speculate that the liquid lifetime of smaller radii filaments may be shorter than larger radii because of the filament substrate contact area to volume ratio. This could be a contributing factor as to why we experimentally see a decrease in retraction velocity at smaller radii (see Figure 3), where theory and simulation predict the opposite trend.

With respect to the behavior of the model, examination of eqs 6, 8, and 10 reveals the effects that the temperature-dependent viscosity and surface tension have on the predicted l_c . Nickel's surface tension decreases with temperature in a linear fashion, $\sigma(T) = 1.78 - 3.3 \times 10^{-4}(T - T_m) \text{ N m}^{-1}$,¹⁸ and viscosity also decreases with temperature, $\mu(T) = 3.4/(T - 995) \text{ Pa s}$, but more dramatically than the surface tension. As surface tension decreases at higher temperatures, it has the effect of pushing l_c to longer lengths. Conversely, decreasing viscosity at higher temperature results in shorter l_c . When both material properties are allowed to vary simultaneously, as in Figure 5a,b, clearly viscosity has greater influence for a given temperature increase, resulting in shortened l_c . However, the magnitude of change in the solutions for l_c at higher temperatures is not as dramatic for the visco-inertial case as it is for the viscous. In the visco-inertial regime the temperature-dependent material properties largely balance each other out; surface tension has a higher power dependence than viscosity in this regime.

Increasing the laser fluence increases the average temperature of a filament, leading to a longer liquid lifetime and a reduced average viscosity and surface tension. Figure 6 is a plot of the

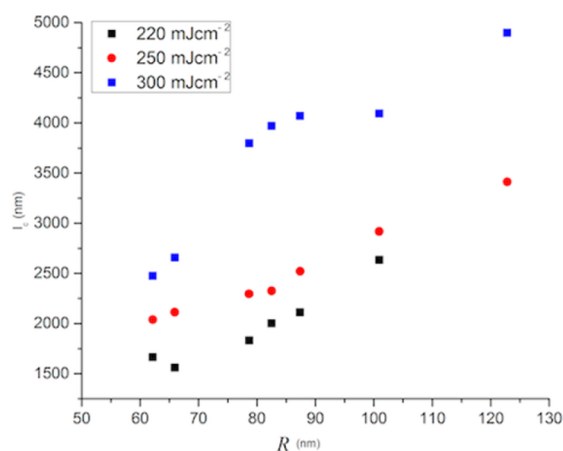


Figure 6. Critical lengths as a function of filament radius area for a 20 nm thick Ni film irradiated at three laser fluences: 200, 250, and 300 mJ cm^{-2} . The longer l_c at higher laser fluence are attributed to higher retraction velocities and longer liquid lifetimes at elevated temperature.

measured l_c for a 20 nm thick Ni TFS irradiated at three different laser fluences, which illustrates that l_c increases with increased laser fluence. As noted above and seen in Figure 5 (illustrated by the analytical model plots for l_c), for a constant retraction velocity, higher temperature is expected to decrease the critical breakup length. This is contrary to the experimental

results seen in Figure 6. However, not accounted for in the governing equation, eq 6, for the competition between the collapse and R–P breakup is the temperature-dependent retraction velocity. We attribute the longer l_c at higher laser fluence to two effects: (1) longer liquid lifetimes at higher temperature and (2) higher retraction velocities due to decreased average viscosity. As will be shown below, the VoF simulations reveal that the solidification of the filament quenches the inertia of the dynamic collapse. For larger radii filaments, that require multiple laser pulses, this decreases the average velocity and leads to a shortening of l_c . For example, at 1728 K, VoF simulations reveal that solidification reduces the average velocity by 40%.

4.2. VoF Simulations. Here, we computationally investigate the dependence of the critical length on the filament radius of curvature when varying the liquid lifetime. Initially, a semicylindrical liquid filament with a cross-sectional area of $C_A = hw$ is placed on a solid surface, with an imposed contact angle of 90° .

We recall that in between laser pulses the liquid metal filament solidifies. We model solidification by simply zeroing the fluid velocity field in the evolving filament after a specified liquid lifetime, t_l , and then continue the evolution, assuming that there is no evolution while the filament is in a solid state. Figure 7 demonstrates the effects of varying the liquid lifetime

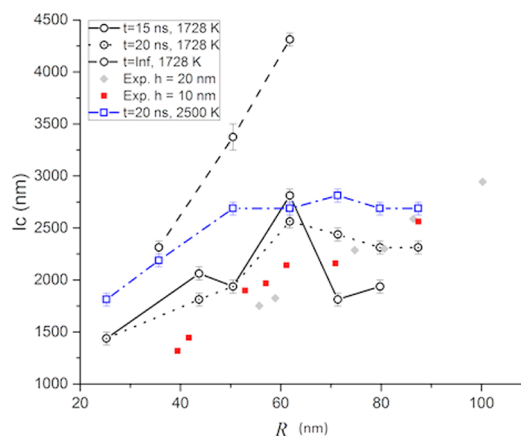


Figure 7. Comparison of the VoF simulations with experimental measurements for l_c as a function of filament radius R . Triangles show experimentally obtained values for thicknesses of $h = 10$ and 20 nm . Circular symbols show the results of VoF simulations as t_l is varied, with material properties set to be the values corresponding to a temperature of 1728 K. Square symbols represent the VoF results when the material properties are set to be the values corresponding to 2500 K and $t_l = 20 \text{ ns}$. For clarity, solid lines represent the experiments and the dotted lines the simulations.

as well as a comparison with the 10 and 20 nm thick TFS experimental data. When $t_l \rightarrow \infty$ (i.e., no solidification, infinite liquid lifetime), simulations predict longer critical lengths compared to the experiments. The difference is particularly significant for larger values of R . The simulation results with $t_l \rightarrow \infty$ therefore reveal that inertial effects are important. When solidification is included, the resulting values of l_c are much shorter and in good agreement with the experiment. Figure 7 suggests that the simulated liquid lifetimes in the range of $\sim 20 \text{ ns}$ provide the best agreement with the experimental results, which is consistent with the thermal simulations (Figure 2). We note that in the simulations the slip length is fixed to be $\lambda = 20$

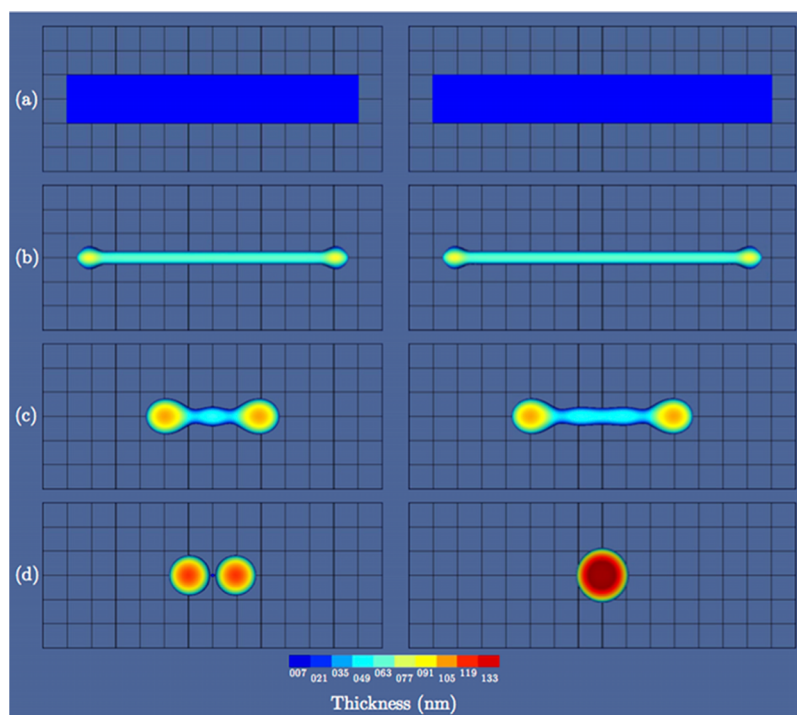


Figure 8. Snapshots of VoF simulation for a Ni filament with initial TFS geometry, $h = 20$ nm, $w = 385$ nm ($R \sim 100$ nm), and $l = 2.31$ μm (left panel) and $l = 2.69$ μm (right panel). (a) Initial geometry ($t = 0$ ns). (b) After the strip has formed a truncated cylindrical filament and the axial ends have begun to retract ($t = 2.5$ ns). (c) At $t = 20$ ns, one simulated liquid lifetime, the filament has “frozen”. (d) The filament either breaks up (left, $t = 39$ ns) and multiple droplet formation occurs or edge droplets coalesce into a single droplet (right, $t = 52$ ns). The VoF simulations capture the dewetting dynamics seen during the experiment in Figure 1c. Note that in the absence of solidification the simulation predicts the filament will collapse into a single drop, for both values of l . Note that in the absence of solidification the simulation predicts the filament will collapse into a single drop, for both values of l .

nm; we carried out an exhaustive study of the effect of slip length on l_c and obtained the best agreement with the experiments with this value.

Additionally, we carry out VoF simulations using the parameters that correspond to higher liquid metal temperature. The parameters used so far are for 1728 K. Now we use the parameters for viscosity, density, and surface tension corresponding to 2500 K. The elevated temperature generally predicts longer l_c (Figure 7), which is consistent with the experimental observation. When the VoF simulations include a change in the temperature-dependent material properties, the apparent viscosity change dominates the reduced surface tension and density and leads to higher retraction velocities (Figure 3), agreeing qualitatively with the experimental results of longer critical lengths at higher laser energy.

Note that the simulation results with solidification included in Figure 7 show that the critical breakup length is not necessarily a monotonously increasing function of R . This unexpected behavior can be attributed to the particular retraction state at which the solidification takes place; Figure 8 shows two representative examples. At early times, both filaments begin to retract with accumulating end droplets (see Figure 8b). At the solidification time (Figure 8c), the central parts of the filaments are characterized by different geometry. For the $l = 2.31$ μm case, the central bulge collapses, and the liquid is transported to the filament ends, leading to breakup and the formation of two droplets. For the $l = 2.69$ μm case, there is no liquid transport from the center bulges to the filament ends, the retraction continues, and a single drop results. This example therefore illustrates that perhaps

surprisingly a breakup may occur for a shorter filament, but not for a longer one. This process also explains why the simulations with $t_l \rightarrow \infty$ lead to a longer l_c . The filament is able to continue retracting without freezing, and so the two filament ends continue to move inward, eventually coalescing to a single droplet. We also note that when ignoring the solidification, the simulated critical lengths compare well with the viscous model presented in the previous section.

4.3. Application. To demonstrate how understanding the collapse versus breakup can be useful, we utilize the insight to facilitate the directed assembly of nanoparticle arrays. Figure 9a–c is a series of composite scanning electron micrographs of a lithographically patterned Ni thin films (background) and the resultant nanoparticle array after ten laser pulses (foreground). The initial, so-called, “square-wave” pattern contains two alternating amplitudes orthogonal to the central axis: (1) A shorter amplitude with a fixed length in Figure 9a–c, which is below the critical length; therefore, these side filaments will collapse to a single droplet. (2) A slightly longer amplitude which progressively increases as noted with the arrows from Figure 9a–c. As the amplitudes of the side filaments increase, a transition is observed: from collapse to a single droplet (Figure 9a) to mixed single and two droplet breakup (Figure 9b) and finally to ordered breakup where two droplets are observed (Figure 9c). The transition occurs at an amplitude of ~ 2.3 μm , which correlates well with the 2.1 μm estimate from the best-fit line of Figure 4a. Thus, the assembly of highly ordered and hierarchical nanoparticle arrays can be realized by understanding the fluid dynamic regimes and instability/transport competitions.

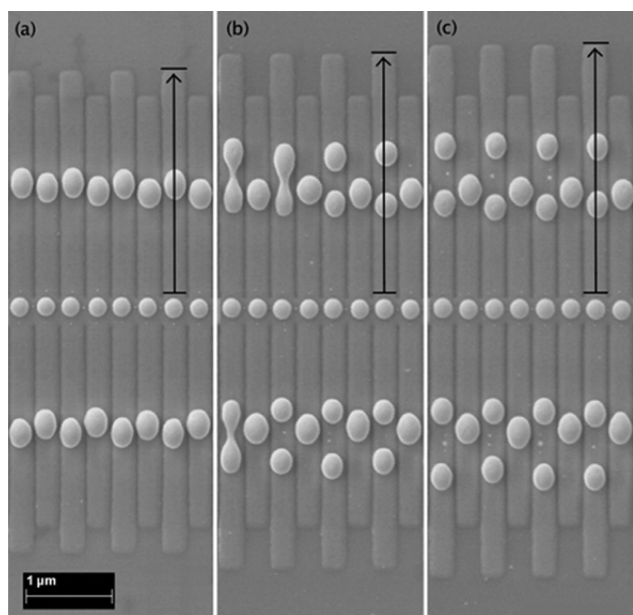


Figure 9. (a–c) Composite SEM images of a lithographically patterned Ni thin film (background), and the resultant nanoparticle array after ten laser pulses (foreground). The transition from single droplet collapse to two droplet breakup is observed in the progression of the larger amplitude side filaments of the “square-wave” pattern.

5. SUMMARY

In this work we studied the critical breakup length, l_c , of partially wetting, liquid metal filaments supported on a solid substrate, under nanosecond laser heating. It was found that filament lengths less than a critical length, $l < l_c$, collapse to a single droplet, and lengths, $l > l_c$, result in breakup into two or more droplets. We show that the critical length can be understood by considering a competition between two fluid dynamic time scales: (1) capillary-induced axial end retraction and (2) filament breakup due to the growth of varicose surface instabilities similar to the R–P mechanism. Furthermore, the competing time scale model was solved for the viscous and the visco-inertial regimes. The visco-inertial regime solution for the breakup length more closely matches the experimental results, which is consistent with the Oh number for the filaments studied. To complement the experimental and model results, fully nonlinear simulations were carried out based on a VoF method. To converge to the experimental length scales, thermal effects like liquid lifetime, solidification morphology, and the temperature-dependent viscosity, surface energy, and density need to be considered. The exploitation of fluid dynamic assembly mechanisms leads to the realization of highly ordered and hierarchical nanoparticle arrays.

AUTHOR INFORMATION

Corresponding Author

*E-mail prack@utk.edu (P.D.R.).

Notes

The authors declare no competing financial interest.

ACKNOWLEDGMENTS

Sample preparation including lithography and metal deposition were conducted at the Center for Nanophase Materials Sciences, which is a U.S. Department of Energy, Office of Science User Facility at Oak Ridge National Laboratory.

C.A.H., P.D.R., and L.K. acknowledge support from NSF Grant CBET-1235710. S.A. acknowledges support from NSF Grant NSF-DMS-1320037. This manuscript has been authored by UT-Battelle, LLC, under Contract DE-AC05-00OR22725, with the U.S. Department of Energy. The United States Government retains and the publisher, by accepting the article for publication, acknowledges that the United States Government retains a nonexclusive, paid-up, irrevocable, worldwide license to publish or reproduce the published form of this manuscript, or allow others to do so, for United States Government purposes. The Department of Energy will provide public access to these results of federally sponsored research in accordance with the DOE Public Access Plan (<http://energy.gov/downloads/doe-public-access-plan>).

REFERENCES

- (1) Atwater, H. A.; Polman, A. Plasmonics for improved photovoltaic devices. *Nat. Mater.* **2010**, *9*, 205–213.
- (2) Wu, J. L.; Chen, F. C.; Hsiao, Y. S.; Chien, F. C.; Chen, P. L.; Kuo, C. H.; Huang, M. H.; Hsu, C. S. Surface Plasmonic Effects of Metallic Nanoparticles on the Performance of Polymer Bulk Heterojunction Solar Cells. *ACS Nano* **2011**, *5*, 959–967.
- (3) Halas, N. J.; Lal, S.; Chang, W. S.; Link, S.; Nordlander, P. Plasmons in Strongly Coupled Metallic Nanostructures. *Chem. Rev.* **2011**, *111*, 3913–3961.
- (4) Le, F.; Brandl, D. W.; Urzhumov, Y. A.; Wang, H.; Kundu, J.; Halas, N. J.; Aizpurua, J.; Nordlander, P. Metallic nanoparticle arrays: A common substrate for both surface-enhanced Raman scattering and surface-enhanced infrared absorption. *ACS Nano* **2008**, *2*, 707–718.
- (5) Rosi, N. L.; Mirkin, C. A. Nanostructures in biodiagnostics. *Chem. Rev.* **2005**, *105*, 1547–1562.
- (6) Anker, J. N.; Hall, W. P.; Lyandres, O.; Shah, N. C.; Zhao, J.; Van Duyne, R. P. Biosensing with plasmonic nanosensors. *Nat. Mater.* **2008**, *7*, 442–453.
- (7) Vo-Dinh, T. Surface-enhanced Raman spectroscopy using metallic nanostructures. *TrAC, Trends Anal. Chem.* **1998**, *17*, 557–582.
- (8) Christopher, P.; Xin, H. L.; Linic, S. Visible-light-enhanced catalytic oxidation reactions on plasmonic silver nanostructures. *Nat. Chem.* **2011**, *3*, 467–472.
- (9) Ozbay, E. Plasmonics: Merging photonics and electronics at nanoscale dimensions. *Science* **2006**, *311*, 189–193.
- (10) Wolf, S. A.; Awschalom, D. D.; Buhrman, R. A.; Daughton, J. M.; von Molnar, S.; Roukes, M. L.; Chtchelkanova, A. Y.; Treger, D. M. Spintronics: A spin-based electronics vision for the future. *Science* **2001**, *294*, 1488–1495.
- (11) Diez, J. A.; Gonzalez, A. G.; Kondic, L. On the breakup of fluid rivulets. *Phys. Fluids* **2009**, *21*, 082105.
- (12) Wu, Y.; Fowlkes, J. D.; Roberts, N. A.; Diez, J. A.; Kondic, L.; Gonzalez, A. G.; Rack, P. D. Competing Liquid Phase Instabilities during Pulsed Laser Induced Self-Assembly of Copper Rings into Ordered Nanoparticle Arrays on SiO₂. *Langmuir* **2011**, *27*, 13314–13323.
- (13) Fowlkes, J. D.; Roberts, N. A.; Wu, Y.; Diez, J. A.; Gonzalez, A. G.; Hartnett, C.; Mahady, K.; Afkhami, S.; Kondic, L.; Rack, P. D. Hierarchical Nanoparticle Ensembles Synthesized by Liquid Phase Directed Self-Assembly. *Nano Lett.* **2014**, *14*, 774–782.
- (14) Roberts, N. A.; Fowlkes, J. D.; Mahady, K.; Afkhami, S.; Kondic, L.; Rack, P. D. Directed Assembly of One- and Two-Dimensional Nanoparticle Arrays from Pulsed Laser Induced Dewetting of Square Waveforms. *ACS Appl. Mater. Interfaces* **2013**, *5*, 4450–4456.
- (15) Mahady, K.; Afkhami, S.; Diez, J.; Kondic, L. Comparison of Navier-Stokes simulations with long-wave theory: Study of wetting and dewetting. *Phys. Fluids* **2013**, *25*, 112103.
- (16) Fowlkes, J. D.; Kondic, L.; Diez, J.; Wu, Y. Y.; Rack, P. D. Self-Assembly versus Directed Assembly of Nanoparticles via Pulsed Laser Induced Dewetting of Patterned Metal Films. *Nano Lett.* **2011**, *11*, 2478–2485.

- (17) Favazza, C.; Kalyanaraman, R.; Sureshkumar, R. Robust nanopatterning by laser-induced dewetting of metal nanofilms. *Nanotechnology* **2006**, *17* (16), 4229–4234.
- (18) Keene, B. J. Review of Data for the Surface-Tension of Pure Metals. *Int. Mater. Rev.* **1993**, *38*, 157–192.
- (19) Lide, D. R. *CRC Handbook of Chemistry and Physics*, 75th ed.; Lewis Pub., 1994.
- (20) Sung, P. K.; Poirier, D. R.; McBride, E. Estimating densities of liquid transition-metals and Ni-base superalloys. *Mater. Sci. Eng., A* **1997**, *231*, 189–197.
- (21) Driessen, T.; Jeurissen, R.; Wijshoff, H.; Toschi, F.; Lohse, D. Stability of viscous long liquid filaments. *Phys. Fluids* **2013**, *25* (6), 062109.
- (22) Davis, S. H. Moving Contact Lines and Rivulet Instabilities 0.1. The Static Rivulet. *J. Fluid Mech.* **1980**, *98*, 225–242.
- (23) Batsanov, S. S. Van der Waals radii of elements. *Inorg. Mater.* **2001**, *37*, 871–885.
- (24) Brochard-Wyart, F.; Redon, C. Dynamics of Liquid Rim Instabilities. *Langmuir* **1992**, *8*, 2324–2329.
- (25) Redon, C.; Brochardwyart, F.; Rondelez, F. Dynamics of Dewetting. *Phys. Rev. Lett.* **1991**, *66*, 715–718.
- (26) Popinet, S. An accurate adaptive solver for surface-tension-driven interfacial flows. *J. Comput. Phys.* **2009**, *228*, 5838–5866.